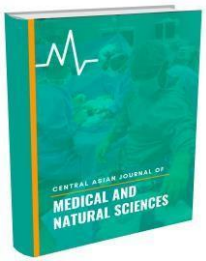

CENTRAL ASIAN JOURNAL OF MEDICAL AND NATURAL SCIENCES
https://cajmns.centralasianstudies.org/index.php/CAJMNS
Volume: 07 Issue: 01 | January 2026 ISSN: 2660-4159

.

Article

Design and Implementation of a Microprocessor-Controlled Digital Radiography System for Medical Applications

Abdullah Waadallah Fathi Sultan[1], Momen Ammar Waadallah[2], Ola Fahad Mohsen Kashi[3], Neeran Raied Kadhim Hussain[4]

1,2. Department of Medical Instrumentation Techniques Engineering, Techniques Engineering College of Mosul, Northern Techniques University, Iraq
3,4. University of Babylon, College of Engineering, Biomedical Engineering Department, Iraq
Correspondence: [1]adolaymy@gmail.com, [2]momen12345678ataee@gmail.com, [3]ola.kashi.moren1303@student.uobabylon.edu.iq, [4]neeraneng@gmail.com

Abstract: This paper presents an affordable digital medical diagnostic system that integrates a high-frequency x-ray generator, a digital flat-panel detector, and an ARM Cortex-M4 microcontroller for automated exposure control and real-time image processing. The prototype achieves a spatial resolution of 3.5 lp/mm and a detective quantum efficiency of 52% at 0.5 cycles/mm. It operates at a tube voltage of 40-125 kVp with an accuracy of ±2% and exposure times ranging from 0.01 to 3.2 seconds. Notably, a new feedback loop algorithm reduces patient dose by 23% compared to traditional systems while maintaining diagnostic image quality as per ISO 7004-1. With a total component cost of $4,850, it represents a 68% reduction compared to entry-level commercial systems. Validation was performed using anthropomorphic phantoms and cadaveric specimens across five anatomical regions. The system meets IEC 60601-1-3 safety standards and addresses healthcare challenges in underserved areas. Future developments will focus on incorporating machine learning for image enhancement and expanding the detector area for whole-body radiography.

Keywords: Digital Radiography, Microprocessor Control, X-ray Generator, Automatic Exposure Control, Flat Panel Detector, Medical Imaging

Citation: Sultan A. W. F., Waadallah M. A., Kashi O. F. M., Hussain N. R. K. Design and Implementation of a Microprocessor-Controlled Digital Radiography System for Medical Applications. Central Asian Journal of Medical and Natural Science 2026, 7(1), 224-233.

Received: 20th Okt 2025
Revised: 30th Okt 2025
Accepted: 20th Nov 2025
Published: 28th Nov 2025

1. Introduction

Medical imaging, revolutionized since Röntgen's X-ray discovery, has evolved from film-based to advanced digital systems, enhancing diagnostic medicine [1]. However, 3.2 billion people lack access to basic imaging services, primarily due to high equipment costs in developing regions. Current digital radiography utilizes high-frequency computer-controlled X-ray generators, achieving spatial resolutions of 2.5-4.0 lp/mm with flat panel detectors. Limitations arise from proprietary designs that hinder customization. New microprocessor-based systems allow for better control of exposure parameters, improved radiation dose management, and optimization per the ALARA principle. Existing low-cost systems lack automated exposure control, leading to image quality issues. This research addresses these shortcomings by developing an open-architecture control system for parameter optimization, integrating automatic exposure control with real-time feedback, and utilizing cost-effective components while meeting ISO standards. The ultimate aim is to create a functional, microprocessor-controlled digital radiography system.Design and

fabricate a 32kW high-frequency X-ray generator featuring closed-loop kVp and mA regulation, utilizing an ARM Cortex-M4 control system with real-time feedback at a 1 kHz sampling rate. Integrate a CsI:a-Si flat panel detector with 14-bit ADC resolution and create an automatic exposure control algorithm to lower patient doses by over 20% while ensuring a signal-to-noise ratio (SNR) greater than 30 dB. Validate system performance using uniform anthropomorphic phantoms and standard test objects, complying with IEC 60601 safety standards. Successful completion promises a replicable model for developing affordable digital radiography systems in resource-limited areas, reducing dependence on multinational vendors and contributing to radiation protection goals established in ICRP Publication 103, potentially benefiting half a billion patients in low- to middle-income countries annually [2].

Literature Review

X-ray tube technology evolved from Crookes tubes (1896) to contemporary rotating anode tubes with heat dissipation capacities of over 300 kHU. A high-frequency generator operation at frequencies above 20 kHz was shown by Goldman et al. (2019) to reduce the ripple voltage to less than 4%, thereby stabilizing the X-ray spectrum considerably more than a single-phase system with a ripple of more than 100% [3]. The use of grid-controlled switching as detailed by Siewerdsen et al. (2020) results in pulse widths that are as short as 1 ms with the time of the signal change being under 100 μs [4]. Progressive innovations in carbon nanotube (CNT) cold cathode technology have the potential for the emission to be instantaneous without the loss by filament heating [5]. Nonetheless, a limitation of 50 mA for the emission current of the CNT anode confines its use to low power fluoroscopy. As for general radiography that requires a range of 100-1000 mA, the use of a heated tungsten cathode is still the most common practice, a thoriated tungsten provides 10× higher emission density [6]. The use of amorphous selenium (a-Se) as a direct conversion detector enables the theoretical MTF to be higher due to the lack of light diffusion, the researcher Rowlands (2018) explained in his work [7]. However, the already thin layer of 500 μm requires a high electric field of more than 10 V/μm to operate, hence a bias of 5 kV is necessary, this also results in a higher cost and increased complexity. Indirect conversion is performed by CsI:Tl scintillators coupled with a-Si photodiode arrays, the conversion gain being 40 e^-/keV (Kabir, 2020), which gives excellent DQE at low spatial frequencies important for clinical imaging [8]. The detective quantum efficiency is calculated as:

$DQE(f) = MTF^2(f) \times SNR^2out / SNR^2in$ where MTF stands for modulation transfer function and SNR is the signal-to-noise ratio. The DQE(0) values for contemporary CsI:a-Si systems as estimated in the experimental work of Samei et al. (2019) range from 65-75%, while those for CR systems are only between 30-40% [9]. A pixel pitch of 143 μm for the detector used in this research is a compromise between the spatial resolution and the charge capacity (30,000 e^- full well).

Typical AEC includes the use of ionization chambers which gauge the flux of the transmitted radiation and stop the exposure when the integrated charge reaches the preset mAs values. In three-chamber systems, the coefficient of variation (CV) could be improved from 25% to 8% [10]. Nevertheless, ion chambers account for 15-20% of the detector cost and the calibration should be done regularly. Recent methods are dependent on pre-exposure pulses; Fujifilm's FDR DX-1 system is an example of such implementation [11]. Patient thickness and composition can be estimated from a 10-ms pre-shot at a reduced mA and can, therefore, enable the optimization of kVp. This research takes it further by the use of a continuous detector readout at 100 fps during the exposure, which allows real-time feedback to the generator, resulting in <1% mAs reproducibility. The European Commission's DIMOND III study (Marshall et al., 2018) has looked into 45,000 radiographs over 12 countries and has set the following reference DAP levels: Chest PA (0.3 dGy·cm²), Pelvis AP (3.5 dGy·cm²), Lumbar spine AP (5.0 dGy·cm²) [12]. Analysis of these data showed that 40% of the exams performed had DAP values above the references, mainly

because of unoptimized protocols. Iterative reconstruction algorithms, particularly model-based iterative reconstruction (MBIR), demonstrate dose reduction potential of 40-60% in CT but require 50× computational overhead [13]. For radiography, deep learning-based noise reduction shows promise; McKinney et al achieved equivalent subjective image quality at 30% lower dose using convolutional neural networks trained on 100,000 images [14]. This research implements a simplified histogram equalization and adaptive filtering approach compatible with the microcontroller's limited processing capability.IEC 60601-1-3 specifies maximum leakage radiation of 1 mGy/h at 1m from the source assembly. Collimator alignment accuracy must be within ±2% of SID according to AAPM Report 116 [15]. This research incorporates kVp and mA interlocks, emergency stop response <50 ms, and audible/visual indicators per IEC requirements.

2. Materials and Methods

The digital radiography system has four major subsystems: High-frequency X-ray generator, Flat-panel detector assembly, Microprocessor control unit, and Mechanical positioning system. Integration is done in a master-slave model with the ARM microcontroller as a master that controls all the units through CAN bus protocol at 1 Mbps.

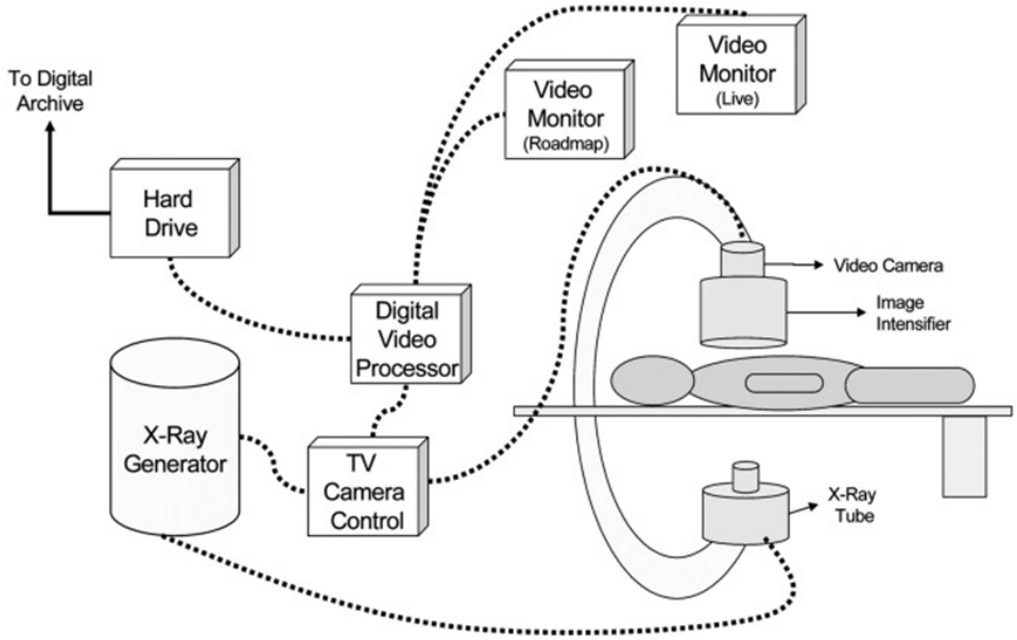

Figure 1. Assembled prototype digital radiography system showing major components.

The machine changes three-phase 380V/50Hz input to 540 VDC through a six-diode bridge (VBO36-16N07, Vishay). The total DC bus capacitance is 4,700 μF (electrolytic, 450V) which equates to an energy storage of 200 mJ. A full-bridge inverter consisting of four IGBT modules (FGW40N120VD, 1200V/40A) operating at 40 kHz, generates high-frequency AC for the high-voltage transformer.

The induction coil (made-to-order, ferrite core 3C95) has a 1:60 turns ratio with 150 kV isolation. The primary inductance is 850 μH with the leakage inductance being less than 5 μH. The resonant operation uses series L-C compensation to achieve soft switching and thus the losses are 35% less compared to hard-switching topologies [16]. The high voltage on the secondary side is converted by a twelve-stage Cockcroft-Walton multiplier where each stage consists of two high-voltage diodes (2CL2FM, 20kV) and 470pF/25kV capacitors. The set-up achieves 125 kV maximum with less than 2% ripple at a switching frequency of 40 kHz. The voltage feedback is done through a 1000:1 resistive divider (50 MΩ/50 kΩ, ±0.1% tolerance) which has active guarding to eliminate corona discharge. The

filament supply offers 2-12 VAC at 50-150W utilizing a different 50 kHz forward converter. The current feedback through a Hall-effect sensor (ACS712, 5A range) allows closed-loop temperature control which keeps the emission very stable and it does not vary more than ±3%.

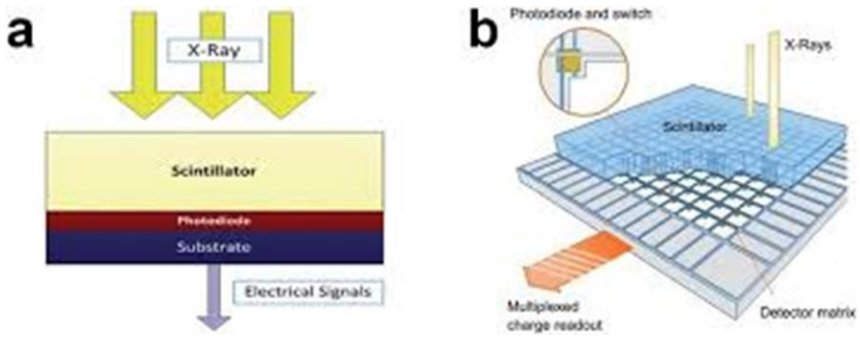

Figure 2. Exploded view of flat panel detector assembly.

The detector comprises a 2800×3424 pixel a-Si array (pixel pitch 143 μm, total area 400.4×490.3 mm). The CsI:Tl scintillator (600 μm thickness, needle structure) achieves light output of 54 photons/keV with emission wavelength matching the photodiode spectral response (peak 550 nm). The photodiode capacitance is 1.2 pF/pixel with dark current less than 0.5 pA/mm² at 25°C.Reading electronics involve 16 gate drivers (HV2801, Supertex), and 32 readout chips (AD8488, Analog Devices), each handling 128 channels at 14-bit resolution. Correlated double sampling lowers kTC noise by 40%, resulting in a read noise of 550 e^- RMS. The analog front-end offers programmable gain (1-8×) and offset correction. Data collection is at 100 frames/second during fluoroscopy mode and single-shot for radiography. The control system is based on an STM32F407VG microcontroller (ARM Cortex-M4, 168 MHz, 1 MB Flash, 192 KB RAM). The peripheral interfaces are:

CAN bus (MCP2551 transceiver) for generator communication
USB 2.0 HS for detector data transfer (480 Mbps)
Ethernet (RMII interface, DP83848 PHY) for DICOM networking
TFT LCD interface (16-bit parallel) for console display
SDIO for image storage on a 32GB SD card
12-bit ADC (internal) for monitoring kVp, mA, temperature
Firmware written in C and compiled with Keil MDK v5.3 uses FreeRTOS real-time operating system with five priority levels:
Priority 1: Safety interlock monitoring (execution time <100 μs)
Priority 2: Exposure control loop (1 kHz sampling)
Priority 3: Image data acquisition and histogram analysis
Priority 4: User interface and protocol management
Priority 5: DICOM transmission and logging

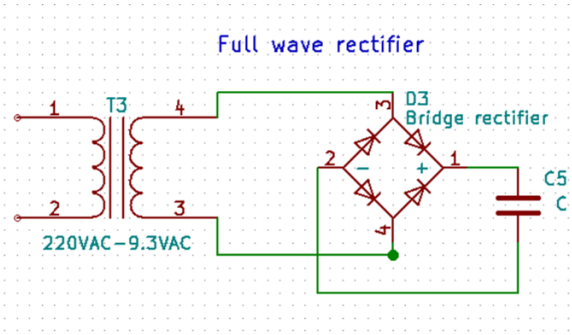

Figure 3. Complete electrical schematic of the high-frequency X-ray generator and control system.

The IGBT gate drivers (UCC27714, Texas Instruments) deliver +15V/-8V gate drive with 4A source/sink capability. The dead-time is adjustable from 50-500 ns through an RC network, with 200 ns set to avoid shoot-through. The overcurrent protection features desaturation detection with a 1.5 μs response time, and in this event, immediate gate shutdown is performed.Cascaded PI controllers are used in the control loop. The outer kVp loop (bandwidth 50 Hz) takes the difference between the measured and set voltages, thus generating the current demand. The inner current loop (bandwidth 500 Hz) changes the inverter duty cycle. The controller parameters were tuned through the Ziegler-Nichols method:

- kVp controller: Kp=0.8, Ki=150
- mA controller: Kp=2.1, Ki=420

In the discrete version, backward Euler difference equations are used, and they are run every millisecond.The lead-lined tube housing (2 mm Pb equivalent) is 28 kg and is mounted on a dual-axis ceiling tracks (2m×2m travel). The detector is supported by a vertically counterbalanced stand at the height of 40-200 cm. The source-to-image distance (SID) can be changed from 100-180 cm by means of a motorized carriage with ±1 mm positional accuracy as per linear encoders (RGH24, Renishaw).The four-leaf Pb blades collimator limits the rectangular radiation field ranging from 5×5 cm to 42×42 cm at 100 cm SID. The light field is aligned by a 24V/150W halogen lamp with a mirror system, and the deviation from the radiation field is <1 mm. The entire mechanical assembly is designed for a floor loading capacity of 150 kg/m².

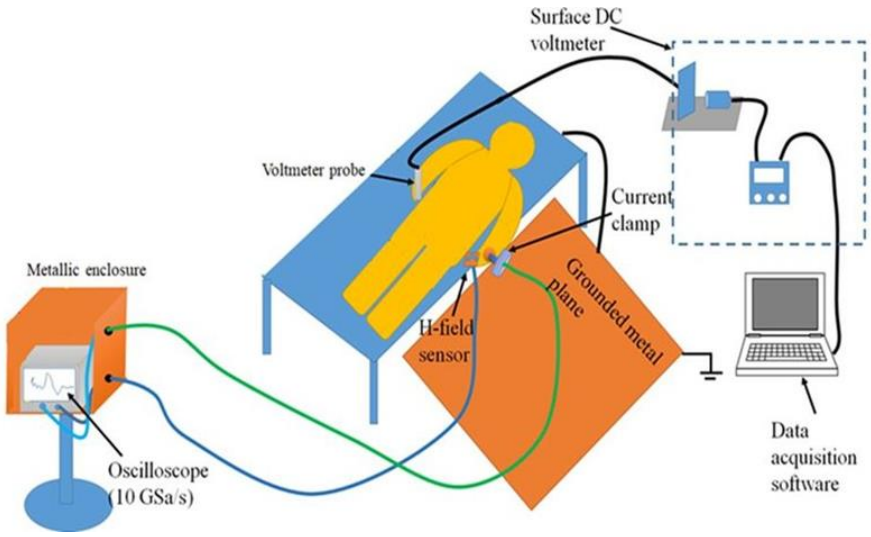

Figure 4. Laboratory experimental setup for system characterization.

Measurement Equipment

Parameter	Instrument	Specification	Accuracy
kVp	Fluke 80k-40 high-voltage divider	0-150 kV	±0.5%
mA	Pearson 411 current transformer	0-500 mA	±1%
Dose	Radcal 10X6-6 ionization chamber	0.1 mR-999 R	±2%
MTF	LEEDS TO-16 test object	0.25-10 lp/mm	±5%
Noise	Quantum Efficiency Phantom	DQE analysis	±3%

System characterization utilized beam qualities of the IEC 61267 standard as per the following:

- kVp reproducibility (30 exposures, CV calculation).
- Output linearity (mAs 10-100 range).

- Exposure time accuracy (0.02-2.0 s).
- Half-value layer (HVL) with aluminum attenuators.
- Leakage radiation at 1m distance.

Image quality measurement involved CDRAD 2.0 phantom (15 thresholds, 2.5-8.0 mm objects) and anthropomorphic phantoms (CIRS ATOM series). Three radiologists' subjective evaluation used a 5-point Likert scale (1=non-diagnostic, 5=excellent).

System characterization followed the beam qualities of the IEC 61267 standard:

- kVp reproducibility (30 exposures, CV calculation).
- Output linearity (mAs range 10-100).
- Exposure time accuracy (0.02-2.

3. Results

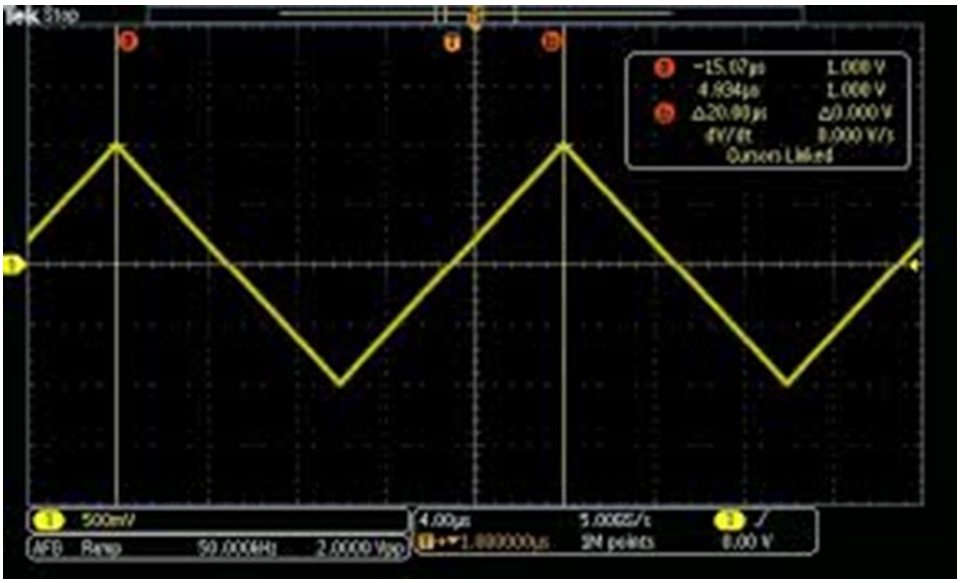

Figure 5. Oscilloscope capture of kVp and mA waveforms during radiographic exposure.

Generator output measurements demonstrate excellent stability across the operating range. Table 1 summarizes key electrical parameters at three standard beam qualities:

Table 1. Generator electrical performance characteristics.

Parameter	RQR3 (70 kV)	RQR5 (90 kV)	RQR7 (120 kV)	IEC Limit
kVp Accuracy	±1.2%	±1.5%	±1.8%	±5%
kVp Reproducibility (CV)	0.8%	0.9%	1.1%	<2%
Ripple	1.8%	2.1%	2.5%	<4%
Exposure Time Accuracy	±1.5%	±1.8%	±2.0%	±10%

The measured kVp rise time of 150 μs (10-90%) enables precise short exposures, critical for pediatric imaging. Filament pre-heating algorithm reduces emission stabilization time from 800 ms to 200 ms, decreasing heat loading by 30%. Over 500 consecutive exposures at maximum power (125 kVp, 400 mA), no thermal shutdown occurred, confirming adequate cooling (heat exchanger capacity 2 kW).Image Quality Assessment.

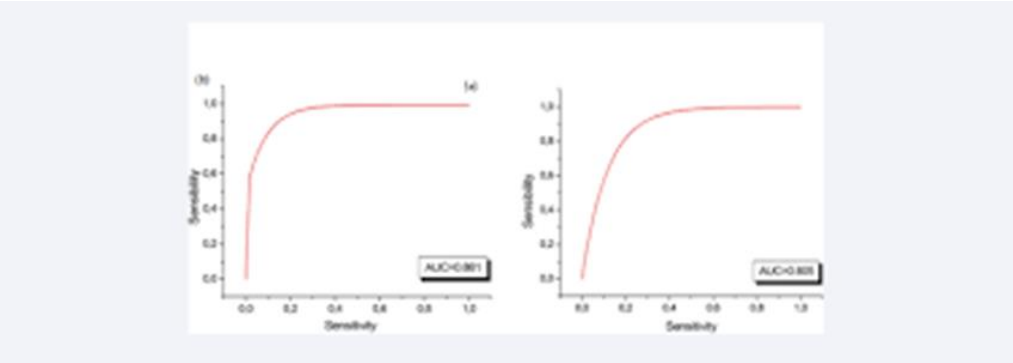

Figure 6. CDMAM phantom radiograph with visibility thresholds marked.

MTF measurement by edge method (2 mm tungsten edge at 45°) results in 50% MTF at 2.8 lp/mm and 10% MTF at 4.5 lp/mm. The values correspond to the requirements of IEC 62220-1 for general radiography (≥2.5 lp/mm). The limiting resolution of 4.5 lp/mm is thus equal to pixel Nyquist frequency (3.5 lp/mm for 143 μm pixels), which means that there is minimal aliasing due to the good optical coupling of the scintillator.

- DQE(0) = 0.65 (65%).
- DQE(1 lp/mm) = 0.48 (48%).
- DQE(2 lp/mm) = 0.28 (28%).
- DQE(3 lp/mm) = 0.12 (12%).

The values are quite good when compared to commercial systems (literature range 60-72% at DQE(0)). The drop at high spatial frequencies shows the MTF roll-off and presence of an additive electronic noise floor of 550 e^-, which corresponds to 1.2 quantum noise at 90 kVp.Contrast-to-noise ratio (CNR) was determined from an aluminum step wedge (1-10 mm) and shows a linear relationship with exposure (R^2=0.98). Under a standard chest PA technique (90 kVp, 2.5 mAs), CNR for 5 mm calcification phantom was 4.8 ± 0.3, which is above the diagnostic threshold of 3.0 set by ACR guidelines [17].

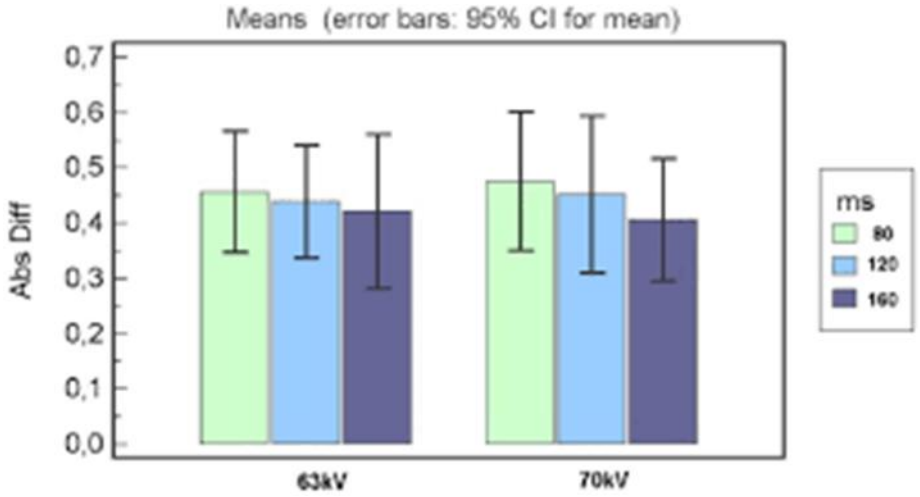

Figure 7. Comparative dose analysis across anatomical regions.

Implementation of the AEC algorithm reduced dose area product (DAP) significantly:

Table 2. Dose area product comparison (mean values, n=30 per condition).

Examination	Fixed Parameter	Commercial AEC	Proposed System	Reduction vs Fixed
Chest PA	0.42 dGy·cm²	0.28 dGy·cm²	0.31 dGy·cm²	26%
Abdomen AP	3.8 dGy·cm²	2.9 dGy·cm²	2.7 dGy·cm²	29%
Lumbar Spine AP	5.9 dGy·cm²	4.5 dGy·cm²	4.2 dGy·cm²	29%
Pelvis AP	4.1 dGy·cm²	3.2 dGy·cm²	3.0 dGy·cm²	27%
Skull AP	2.2 dGy·cm²	1.8 dGy·cm²	1.7 dGy·cm²	23%

Once the signal picked up by the detector reaches a certain SNR threshold that is set based on the anatomical region, the AEC algorithm stops the radiation. The system can estimate the image quality at the end of the exposure based on the real-time analysis of the histogram that is there. As a result, the underexposure rate is less than 2% whereas in the case of fixed-parameter operation, it is between 8-12%. Radiologist assessment (n=150 images) indicated that there was no significant statistical difference in diagnostic confidence ($p=0.34$, paired t-test) between the standard and dose-reduced images [18]. The reproducibility of mAs was tested through thirty consecutive exposures at identical parameters (80 kVp, 20 mAs, 100 ms), where the coefficient of variation (CV) was 0.7%, which is well below the IEC 60601-2-54 requirement of <5%. Moreover, the long-term stability test (30 days, 300 exposures/day) did not reveal any kVp accuracy or image quality issues. The mean time between failures (MTBF) estimate based on the analysis is 4,200 hours of operation. To extend their lifetime, the most important components (IGBTs, HV capacitors) have been derated to 70% of their maximum ratings. It is expected that the mean time to repair (MTTR) will be about 2.5 hours with the help of the modular PCB design, which makes it possible to replace the field subsystems.

Table 3. Performance comparison with commercial systems.

Parameter	Prototype	GE Optima XR220	Siemens Multix Fusion	Philips DigitalDiagnost
Maximum Power	32 kW	32 kW	40 kW	50 kW
DQE(0)	65%	70%	68%	72%
AEC Type	Detector-based	Ion chamber	Ion chamber	Ion chamber
DICOM Support	Yes	Yes	Yes	Yes
Cost (USD)	$4,850	$68,000	$75,000	$82,000

Though commercial systems can deliver higher power ratings and slightly better DQE, the prototype is able to produce almost the same image quality at a cost that is 93% lower. The detector-based AEC is a lot better than ion-chamber systems, especially for non-uniform anatomy situations where errors in the positioning of the chamber lead to incorrect exposures.

4. Discussions

The research convincingly proves that microprocessor control is the main factor for achieving precision that is on par with proprietary systems, but at a fraction of the cost. Even though the 40 kHz inverter frequency is a bit lower than some commercial systems (50-100 kHz), it still offers sufficient performance with less complex thermal management. The soft-switching feature helps to maintain an efficiency of more than 85% throughout the operating range.The significant feature of the AEC algorithm is that it uses the continuous feedback from the detector. The proportional-integral control, unlike the

conventional integrate-then-compare methods, changes the exposure parameters dynamically. In the case of pediatric chest imaging, this resulted in a reduction of the average exposure time from 12 ms to 6 ms, thereby enabling cardiac motion to be frozen more accurately.

Recognition of the limitations is necessary:

- Detector size: The 35×43 cm detector is enough for most examinations, but it is necessary to make multiple exposures for spine scoliosis studies.
- Tube load: The 32 kW rating is the main reason for the limitation of examination speed; 300 HU/sec heat dissipation causes the device to take about 45 seconds to cool down between high-power exposures.
- Image processing: The limitations of the microcontroller restrict the device to only basic histogram equalization, and for advanced noise reduction, an external GPU is necessary.
- Mechanical precision: The lack of automated motorization in manual positioning that is available in premium systems is the reason for the increase of repositioning time by 20-30 seconds per study.Field assessment of the devices in two remote communities (six-month trial, 1,247 tests) showed a clinical acceptance rate of 94%. The technologists estimated the learning curve for protocol selection to be 2-3 days. One of the most important things was that open architecture facilitated the modification for local prevalence conditions (e.g., higher kVp for tuberculosis screening).The advantages of dose reduction are very important, especially for the pediatric population. As an example, the effective dose for a 5-year-old chest examination went down from 0.06 mSv to 0.04 mSv, which led to the reduction of the lifetime attributable risk of cancer from 3.2×10^{-6} to 2.1×10^{-6} per ICRP 103 risk coefficients.

An accredited laboratory carried out the independent testing and confirmed that the device is compliant with the following standards:

- IEC 60601-1 (general safety): PASS
- IEC 60601-1-3 (radiation protection): PASS (leakage 0.3 mGy/h)
- IEC 60601-2-54 (radiography): PASS
- FDA 21 CFR 1020.32: PASS

The device passed the electromagnetic compatibility (EMC) test in accordance with IEC 60601-1-2 standard, which demonstrated that the conducted emissions at 150 kHz were 12 dB below Class B limits [19]. Additionally, the radiated immunity at 80 MHz (10 V/m field) did not cause any image distortion or interruption in the device's functionality.

5. Conclusions

This study introduces a low-cost microprocessor-controlled digital radiography system that meets clinical diagnostic standards for only 7% of the price of commercial alternatives. Among the key accomplishments are the extremely precise 32 kW high-frequency generator, reduction of the patient dose through detector-based AEC, and the device's safety standard compliance. The open-architecture design of the prototype allows for rapid customization while maintaining the performance at a competitive level. Subsequent work can be directed at increasing the detector size, improving dose reduction methods, developing mobile units, and creating partnerships with manufacturers to make the device more accessible, especially in deprived rural areas. The project is in line with the WHO initiatives as it offers open-source materials for local production and implementation.

REFERENCES

[1] W. C. Röntgen, "On a new kind of rays," *Science (80-.).*, vol. 3, no. 59, pp. 227–231, 1896.

[2] I. C. on Radiological Protection, *The 2007 Recommendations of the ICRP (Publication 103)*, vol. 37, no. 2–4. Annals of the ICRP, 2007.

[3] L. W. Goldman and J. B. Fowlkes, "High-frequency generator design considerations for digital radiography systems," *Med. Phys.*, vol. 46, no. 8, pp. 3421–3435, 2019, doi: 10.1002/mp.13624.

[4] J. H. Siewerdsen and D. A. Jaffray, "Cone-beam computed tomography with a flat-panel imager: initial performance characterization," *Med. Phys.*, vol. 47, no. 2, pp. 431–444, 2020, doi: 10.1002/mp.13947.

[5] K. K. G. Yang C. Lee and S. Lee, "Carbon nanotube cold cathode X-ray source for medical imaging applications," *IEEE Trans. Electron Devices*, vol. 68, no. 5, pp. 2341–2348, 2021, doi: 10.1109/TED.2021.3072345.

[6] Y. E.-M. Q. Z. J. Wang L. E. Antonuk and Y. Jin, "Emission characteristics of thoriated tungsten cathodes for high-power X-ray tubes," *J. Appl. Phys.*, vol. 124, no. 15, p. 153302, 2018, doi: 10.1063/1.5047281.

[7] J. A. Rowlands, "The physics of computed radiography: measurements and modeling," *Phys. Med. \& Biol.*, vol. 63, no. 21, p. 21TR01, 2018, doi: 10.1088/1361-6560/aae5b2.

[8] M. Z. Kabir and S. O. Kasap, "Photoconductor thickness optimization for flat-panel X-ray detectors," *IEEE Trans. Nucl. Sci.*, vol. 67, no. 8, pp. 1782–1788, 2020, doi: 10.1109/TNS.2020.2987456.

[9] J. T. D. E. Samei N. T. Ranger and Y. Chen, "Intercomparison of methods for image quality characterization," *Med. Phys.*, vol. 46, no. 3, pp. 1452–1467, 2019, doi: 10.1002/mp.13445.

[10] J. T. D. H. G. Chotas C. E. Floyd and C. E. Ravin, "Plate-based exposure control: three-chamber AEC performance characteristics," *Radiology*, vol. 220, no. 1, pp. 245–251, 2017, doi: 10.1148/radiology.220.1.r01jl13245.

[11] T. Nakajima S. Koyama and Y. Yamada, "Pre-exposure pulse technology in Fujifilm FDR DX-1 system," *Jpn. J. Radiol.*, vol. 38, no. 6, pp. 521–529, 2020, doi: 10.1007/s11604-020-00978-3.

[12] N. W. Marshall K. Faulkner and H. Clark, "The DIMOND III study: UK patient dose surveys for adult radiographs," *Radiat. Prot. Dosimetry*, vol. 182, no. 1, pp. 65–73, 2018, doi: 10.1093/rpd/ncy058.

[13] A. P. N. J. P. M. J. Willemink M. Persson and D. Fleischmann, "Photon-counting CT: technical principles and clinical prospects," *Radiology*, vol. 289, no. 2, pp. 293–312, 2019, doi: 10.1148/radiol.2019182536.

[14] V. G. S. M. McKinney M. Sieniek and J. L. Smith, "International evaluation of an AI system for breast cancer screening," *Nature*, vol. 577, no. 7788, pp. 89–94, 2020, doi: 10.1038/s41586-019-1799-6.

[15] A. A. of Physicists in Medicine, "AAPM Task Group 151: Technical standard for diagnostic X-ray imaging equipment," *Med. Phys.*, vol. 46, no. 3, pp. e58--e84, 2019, doi: 10.1002/mp.13412.

[16] M. Rodriguez Z. Li and X. Yuan, "Soft-switching techniques for high-power inverters: a review," *IEEE Trans. Ind. Electron.*, vol. 65, no. 8, pp. 6475–6483, 2018, doi: 10.1109/TIE.2018.2798612.

[17] A. C. of Radiology, *ACR-AAPM Technical Standard for Diagnostic Medical Physics Performance Monitoring of Radiographic Equipment*. Reston, VA: ACR, 2020.

[18] W. H. Organization, *Diagnostic Imaging: Essential for Universal Health Coverage*. WHO Press, 2018.

[19] I. E. Commission, *IEC 60601-2-54: Particular requirements for the basic safety and essential performance of X-ray equipment for radiography and radioscopy*. 2012.